# Thermal Conductivity Enhancement in MoS_{2} under Extreme Strain

Xianghai Meng, Tribhuwan Pandey, Jihoon Jeong, Suyu Fu, Jing Yang, Ke Chen, Akash Singh, Feng He, Xiaochuan Xu, Jianshi Zhou, Wen-Pin Hsieh, Abhishek K. Singh, Jung-Fu Lin, and Yaguo Wang

Phys. Rev. Lett. **122**, 155901 — Published 18 April 2019

DOI: 10.1103/PhysRevLett.122.155901

# Thermal Conductivity Enhancement in $MoS_2$ under Extreme Strain

Xianghai Meng[†1], Tribhuwan Pandey[†2], Jihoon Jeong[1], Suyu Fu[3], Jing Yang[3], Ke Chen[1], Akash Singh[2], Feng He[4], Xiaochuan Xu[5], Jianshi Zhou[4], Wen-Pin Hsieh[6], Abhishek K. Singh[2], Jung-Fu Lin*[3], Yaguo Wang*[1,4]

[†]These authors contributed equally.

[1] Department of Mechanical Engineering, The University of Texas at Austin, 204 E. Dean Keeton St, Austin, TX 78712, USA.

[2] Materials Research Centre, Indian Institute of Science, Bangalore 560012, India.

[3] Jackson School of Geosciences, The University of Texas at Austin, 2305 Speedway Stop C1160, Austin, TX 78712, USA.

[4] Texas Materials Institute, The University of Texas at Austin, 204 E. Dean Keeton St, Austin, TX 78712, USA.

[5] Omega Optics, Inc. 8500 Shoal Creek Blvd., Bldg. 4, Suite 200, Austin, Texas 78757, USA.

[6] Institute of Earth Sciences, Academia Sinica, Nankang, 11529 Taipei, Taiwan

PACS numbers: 63.22.Np, 65.80.Ck

**Keywords:** TMD, thermal conductivity, compressive strain, phonon

**Abstract**

Due to their weak interlayer bonding, van der Waals (vdW) solids are very sensitive to external stimuli such as strain. Experimental studies of strain tuning of thermal properties in vdW solids have not yet been reported. Under ~9% cross-plane compressive strain created by hydrostatic pressure in a diamond anvil cell, we observed an increase of cross-plane thermal conductivity in bulk $MoS_2$ from 3.5 $Wm^{-1}K^{-1}$ to about 25 $Wm^{-1}K^{-1}$, measured with a picosecond transient thermoreflectance technique. First-principles calculations and coherent phonon spectroscopy experiments reveal that this drastic change arises from the strain-enhanced interlayer interaction, heavily modified phonon dispersions, and decrease in phonon lifetimes due to unbundling effect along cross-plane direction. The contribution from the change of electronic thermal conductivity is negligible. Our results suggest possible parallel tuning of structural, thermal and electrical properties of vdW solids with strain in multi-physics devices.

**Main Text**

Strain is an effective tool to tune physical properties in a wide range of materials [1-4]. In transition metal dichalcogenides (TMDs), a family of two-dimensional (2D) van der Waals (vdW) solids, strain can alter the interlayer distance, as well as bond strength, length and angle between the transition metal and chalcogen atoms, modifying the interatomic orbital coupling, interlayer wavefunction overlap and valence band splitting [5-7]. Changes in these physical parameters can modulate electronic and phononic properties to a great extent. For example, the electronic band gap and phonon Raman peaks in TMDs have been shown experimentally very sensitive to strain, with an $A_{1g}$ phonon Raman shift as large as ~5-6 $cm^{-1}/\%$ [8-13]. In traditional mechanical bending/stretching experiments, the 2D materials sit on a flexible substrate and strain is determined

by the elongation or radius of curvature of the substrate [8, 9, 14, 15]. Any slippage across the sample/substrate interface or imperfect strain transfer across layers can introduce large uncertainties. Therefore, the reported values of strain-induced Raman peak shifts using these techniques vary significantly and are sometimes contradictory [8, 10, 16] (Fig. S5). Moreover, strains generated in stretching/bending experiments are typically only less than 4% [8, 17]. Hydrostatic pressure created in a diamond anvil cell (DAC) can generate compressive strain as high as 30% [18, 19], without introducing any damage to the samples. DACs have been extensively used in the geophysics field to simulate the high-pressure environment in planetary interiors [20]. Pressure in a DAC is determined by monitoring the fluorescence peak of a ruby crystal placed adjacent to the sample, with an accuracy better than 1 GPa (Fig. S2). *In situ* high-pressure synchrotron X-ray diffraction (XRD) experiments measure the pressure-induced change in lattice parameters, from which the resultant strain can be determined. The reported Raman peak shifts of 2D materials under strain generated in a DAC are highly consistent among different studies, including our own [21-25] (Fig. S2).

Previous studies demonstrated that with about 9% cross-plane compressive strain, molybdenum disulfide ($MoS_2$), one of the most studied TMD material for novel electronics [26-30], exhibits a semiconductor to metal (S-M) transition [6, 31], with an electrical conductivity enhancement from 0.03 S/m to 18 S/m [19, 21]. Extreme strain should also have a profound impact on phonon transport properties, which can affect the thermal conductivity in $MoS_2$. $MoS_2$ possesses highly anisotropic thermal conductivities along in-plane and cross-plane directions. The reported in-plane thermal conductivity ($\kappa_{//}$) ranges from 35 to 85 $Wm^{-1}K^{-1}$ [32-34] – more than 10x higher than the cross-plane thermal conductivity ($\kappa_{\perp}$ ~2-4.5 $Wm^{-1}K^{-1}$) [32, 35-37]. Small $\kappa_{\perp}$could jeopardize heat dissipation of TMD-based electronics, and techniques to enhance the cross-plane thermal conductivity are required. Previous theoretical studies of strain's effect on thermal conductivity in

66 TMDs have reached inconsistent conclusions [38-42], and experimental studies have not yet been
67 reported. Thus, exploring the tunability of thermal conductivity in TMDs with strain will not only
68 have scientific significance, but also inform thermal management techniques in all TMD-based
69 electronic devices.

70 In this work, a DAC device is integrated into our recently developed picosecond transient
71 thermoreflectance (ps-TTR) system [43] to study strain-tuned cross-plane thermal conductivity ($\kappa_{\perp}$)
72 in bulk $MoS_2$ up to ~19 GPa (over 9% cross-plane strain). We observed roughly a 7x increase of $\kappa_{\perp}$,
73 from 3.5 W $m^{-1}K^{-1}$ at ambient pressure to about 25 W $m^{-1}K^{-1}$ at 19 GPa. First-principles calculations
74 and electrical conductivity measurements suggest that this drastic change arises mainly from the
75 substantially strengthened interlayer force and heavily modified phonon dispersions along the
76 cross-plane direction. The group velocities of coherent longitudinal acoustic phonons (LAP),
77 measured with coherent phonon spectroscopy (CPS), increase by a factor of 1.6 at 19 GPa due to
78 phonon hardening, while their lifetimes decrease due to the phonon unbundling effect. Our findings
79 could be extended to any 2D materials bonded by vdW forces, down to bi-layer systems.

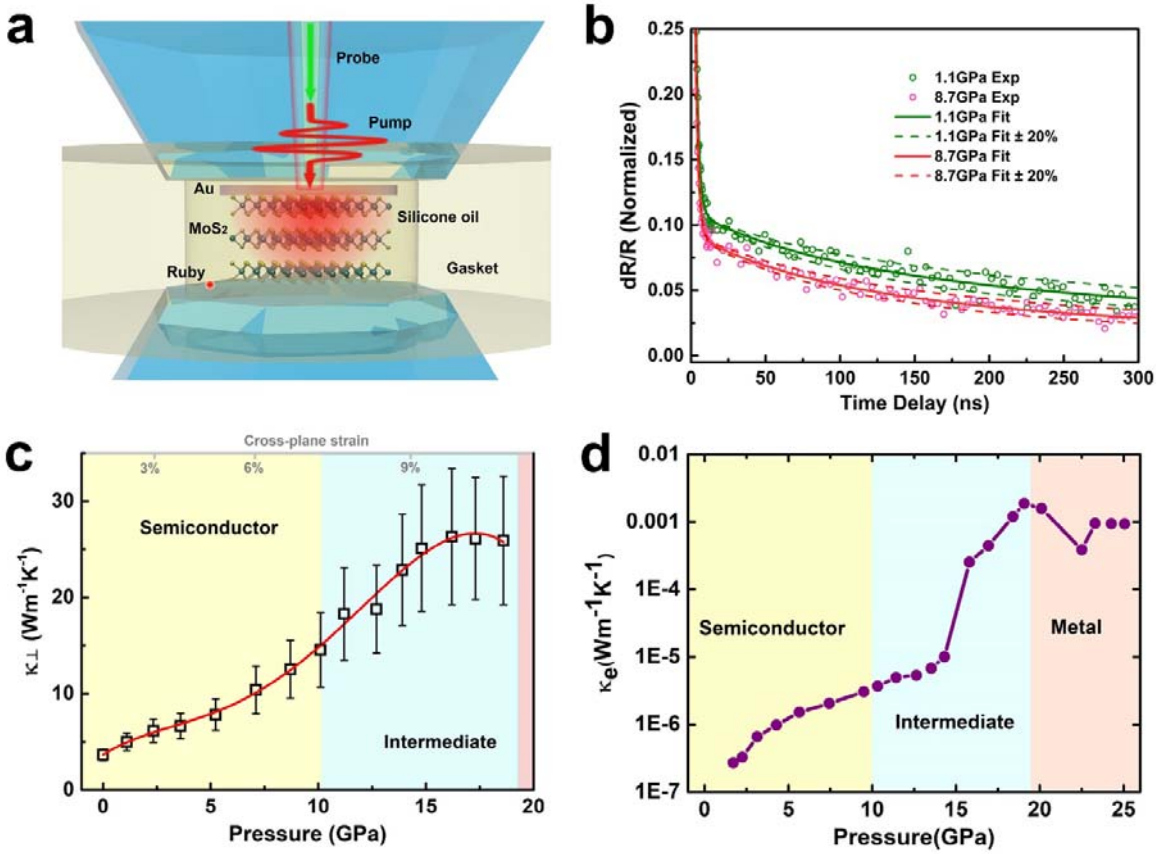


**FIG. 1. Experimental setup, total and electronic thermal conductivity under high pressure. (a)** Schematic of thermal conductivity measurement with a diamond anvil cell (DAC) integrated with a ps-TTR system. **(b)** Experimental data and fitting of ps-TTR measurements at two selected pressures, with ±20% confidence interval shown. **(c)** Extracted cross-plane thermal conductivity (both lattice and electronic) as a function of pressure. The red curve is included only as a guide to the eye. Semiconducting and intermediate regions are labeled based on Ref. [19]. **(d)** Electronic thermal conductivity of $MoS_2$ against pressure, determined from measured electronic conductivity via the Wiedemann-Franz law [19]. Three regions of the semiconductor to metal transition are labeled.

Fig. 1(a) shows a DAC device implemented into our ps-TTR system (Fig. S6). The force exerted by two opposing diamonds is transformed into hydrostatic pressure through the pressure medium: low-thermal-conductivity silicone oil. A ruby crystal placed adjacent to the sample serves as the pressure calibrant [44]. The $MoS_2$ sample used in this study was prepared by mechanical exfoliation, with a thickness of about 20 μm. Raman spectra suggest that our sample remains in the

2-H phase throughout the pressure range measured (Fig. S3). Our pressure-dependent Raman shifts of $A_{1g}$ and $E_{2g}$ phonons agree well with literature data [22, 23] (Fig. S4). A 61-nm thick Au thin film was deposited onto the sample surface to increase the thermoreflection of the probe (532 nm). Fig. 1(b) presents the thermoreflectance spectra at two selected pressures. A one-dimensional (1D) thermal conduction model was used to calculate the time-resolved temperature profile and extract thermal conductivity from experiments:

$$\rho c_p \frac{\partial T}{\partial t} = \kappa \frac{\partial^2 T}{\partial z^2} + \dot{S} \quad (1)$$

In Eqn. 1, $\rho$ is density, $c_p$ is specific heat, $T$ is temperature, $\kappa$ is thermal conductivity and $\dot{S}$ is the heating source term for the pump laser. With a Gaussian laser pulse, the source term takes the form: $\dot{S} = I_0(1-r)\alpha\, exp\left(-\frac{t^2}{\tau^2}\right) exp(-\alpha z)$, where $I_0$ is peak laser intensity, $r$ is reflectivity (0.979 at 1064nm), $\alpha$ is the absorption coefficient of Au at pump wavelength ($8.22\times10^5$ $cm^{-1}$ at 1064 nm), and $\tau$ is the laser pulse width (full width at half maximum, 15 ps). Pump and probe spot sizes are 120 μm and 10 μm ($1/e^2$ diameter), respectively. With a pump pulse energy of 800 nJ, the temperature rise in the Au layer is estimated to be about 9 K. Sensitivity and uncertainty analysis show that temperature profiles are mainly sensitive to $\kappa_{MoS2}$ after 100 ns (Fig. S9). Experimental data up to 300 ns are used for fitting to extract $\kappa_{MoS2}$. Our thermal conduction model considers the silicone oil, Au thin film and $MoS_2$ layers as well as the interfaces between them, though not the diamond, as the sample thickness (20 μm) is much greater than the thermal diffusion length ($D = \sqrt{\frac{\kappa}{C_p} \cdot t_{max}}$ is estimated to be ~ 1.8 μm, if using $\kappa_{MoS2}$= 25 $Wm^{-1}K^{-1}$, $c_p$ = $2.3\times10^6$ $Jm^{-3}K^{-1}$ and $t_{max}$=300 ns). Pressure could strongly affect many thermal parameters in the heat conduction model; however, the major unknowns are $\kappa_{MoS2}$, the interface thermal resistance between silicone oil and Au ($R_{oil/Au}$), and that between Au and $MoS_2$ ($R_{Au/MoS2}$). Values of other parameters at high pressure can be extracted from literature (Fig. S8), or neglected due to the close-to-zero sensitivity compared with $\kappa_{MoS2}$.

(Sections V&VI in the supplemental material [47].)

Plotted in Fig. 1(c) is the pressure-dependent cross-plane thermal conductivity $\kappa_{⊥,total}$ of $MoS_2$ extracted from ps-TTR measurements (see Fig. S10 for pressure-dependent $R_{oil/Au}$ and $R_{Au/MoS2}$ ). At ambient pressure, the measured $\kappa_{⊥,MoS2}$ and interface resistance $R_{Au/MoS2}$ values are $3.5 \pm 0.57$ $Wm^{-1}K^{-1}$ and $82 \times 10^{-9} \pm 14$ $Km^2W^{-1}$, respectively. Our $\kappa_{⊥,MoS2}$ value is within the range of the previously reported results, between $2.0 \pm 0.3$ $Wm^{-1}K^{-1}$[32, 37] and $4.75 \pm 0.32$ $Wm^{-1}K^{-1}$[32, 37]. In literature, a value for $R_{Au/MoS2}$ of $58 \times 10^{-9}$ $Km^2W^{-1}$ was predicted with first-principles calculations [54], consistent with what we have measured [55]. Over the entire pressure range, the Kapitza length ($\Lambda = \kappa_{⊥,MoS2}R_{Au/MoS2}$) is comparable with the thermal diffusion length in the $MoS_2$ layer, and hence our experimental data is sensitive to both $\kappa_{⊥,MoS2}$ and $R_{Au/MoS2}$. (Section V in supplemental material .)The top axis of Fig. 1(c) shows the corresponding strain along the cross-plane direction, which is derived from the pressure-dependent lattice parameters of $MoS_2$ [19] (Fig. S2). $\kappa_{⊥,total}$ exhibits a dramatic change from about 3.5 $Wm^{-1}K^{-1}$ at ambient pressure to about 25 W $m^{-1}K^{-1}$ at 15 GPa, and tends to saturate thereafter. Both $R_{oil/Au}$ and $R_{Au/MoS2}$ increase with pressure, consistent with previous experimental and theoretical works [58-61] (Fig. S10). This ~7x $\kappa_{⊥,total}$ enhancement with pressure has two possible origins: a) enhanced electronic thermal conduction along with S-M transition; b) enhanced phonon contribution due to reduced interlayer distance and modified phonon structure.

Electronic thermal conductivity is related to electrical conductivity. Fig. 1(d) shows the pressure-dependent electronic thermal conductivity converted from electrical conductivity measurements [19] via the Wiedemann-Franz Law: $\kappa_e/\sigma=LT$, where $\sigma$ is electrical conductivity, $L$ is Lorenz number taken as $2.44\times10^{-8}$ $W\Omega$ $K^{-2}$, and $T$ is temperature [62]. $\kappa_e$ increases from about $10^{-7}$ $Wm^{-1}K^{-1}$ at ambient pressure to about $10^{-3}$ $Wm^{-1}K^{-1}$ at 20 GPa due to the closure of the electronic

bandgap at high pressure (S-M transition) [19]. However, compared with the pressure-dependent $\kappa_{\perp,total}$, the contribution from $\kappa_e$ is negligible, accounting for less than 0.01% of the total thermal conductivity. In normal metals, electron thermal conductivity usually dominates heat conduction. For metallic $MoS_2$ [19, 63], the small $\kappa_e$ is attributed to the small electron density of states near the Fermi level. Therefore, the substantial increase observed in $\kappa_{\perp,total}$ should be attributed to the strain-modified phonon properties.

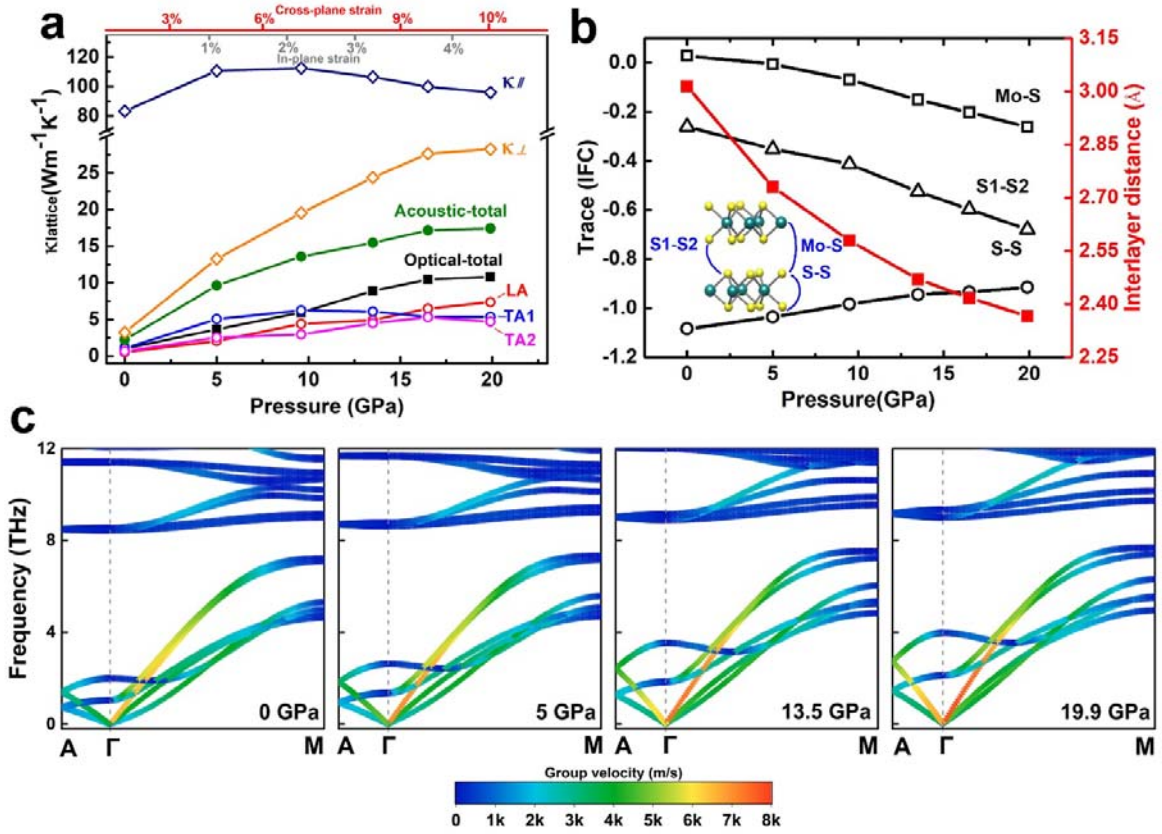


**FIG. 2. Calculated lattice thermal conductivity, interatomic force constant and phonon dispersion curves. (a)** Pressure-dependent in-plane and cross-plane lattice thermal conductivities obtained by first-principles calculations, with contributions to $\kappa_{\perp,lattice}$ from acoustic, optical, longitudinal acoustic (LA) and two transverse acoustic (TA1, TA2) phonon branches. **(b)** Pressure-dependent interatomic force constants of the interlayer Mo-S bond, interlayer S-S (S1-S2) bond and intralayer S-S bond from first-principles calculations. **(c)** First-principles calculations of the pressure induced change of phonon dispersion curves and phonon group velocities in multilayer

$MoS_2$ along both cross-plane (Γ-A) and in-plane (Γ-M) directions. Group velocities are shown using a color gradient, with warmer colors indicating higher group velocities.

Plotted in Fig. 2(a) are the lattice thermal conductivities calculated with density functional theory and Boltzmann's transport equation (Section X in the supplemental material [64]). The calculated pressure-dependent $\kappa_{⊡,lattice}$ increases monotonically from 3.2 $Wm^{-1}K^{-1}$ to 28.3 $Wm^{-1}K^{-1}$, which agrees relatively well with our measured values. The discrepancy in pressure dependence at intermediate pressures may arise from the difference between the actual lattice constants and those optimized in simulations to minimize the total energy. In contrast to $\kappa_{⊡,lattice}$, in-plane thermal conductivity $\kappa_{//,lattice}$ shows only moderate enhancement (< 37%) at lower pressures and reaches a maximum around 5-10 GPa. This trend – an initial increase and subsequent decrease in $\kappa_{//,lattice}$ with pressure – was also predicted with first-principles calculations in monolayer AsP [76], bi-/tri-layer graphene [77], and penta-$SiC_2$ [78]; it was attributed to the competition between decreasing phonon velocity/heat capacity and increasing phonon lifetimes under tensile strain. The dissimilar pressure dependence between $\kappa_{⊡,lattice}$ and $\kappa_{//,lattice}$ comes from the differing compressibility along cross-plane and in-plane directions. The top axis of Fig. 2(a) shows the pressure-induced strain along each direction. Even under hydrostatic pressure, the cross-plane strain generated is more than 10% while in-plane strain is less than 5%. At room pressure, the ratio of $\kappa_{⊡,lattice}$ / $\kappa_{//,lattice}$ is only about 3.9%; at 20 GPa, this ratio becomes 29.4 %. Fig. 2(b) presents the trace of interatomic force constants (IFC) calculated with a first-principles approach for three different types of bonds in $MoS_2$. At ambient condition, the IFC of the interlayer Mo-S bond is positive due to the vdW interaction, which gives the bond an "anti-spring" behavior. With increasing hydrostatic pressure, the IFC of the Mo-S bond becomes negative and increases by about 10 times at 20 GPa, indicating substantially strengthened interaction between interlayer atoms. Similarly, the interlayer S1-S2 bond shows a 2x increase at 20 GPa. In contrast, the intralayer S-S bond exhibits a slight decrease from its ambient value, due to

the already strong covalent bonding among intralayer atoms. Fig. 2(a) also presents the contributions to $\kappa_{\perp,lattice}$ from various phonon branches. One noteworthy feature is that optical phonons account for ~27-38% of $\kappa_{\perp,lattice}$, unlike most common semiconductors, for which the optical phonon contribution is usually negligible. For acoustic phonons, contributions from longitudinal acoustic (LA) and transverse acoustic (TA) branches are comparable.

One important question is whether the interlayer interaction at 20 GPa is still vdW type or not. Our previous work shows that with pressure, electron charges tend to move away from Mo atoms and accumulate at the S atoms in adjacent layers, and electron hybridization takes place between the *p* electrons of S atoms and the *d* electrons of Mo atoms [19]. This charge transfer and hybridization reinforce the interlayer interaction to be much stronger than vdW force, which induces a drastic increase of electrical conductivity. Nevertheless, even at 20 GPa, the interlayer S1-S2 distance is about 2.93 Å, still much longer than that of the S-S dimer (1.8 Å) in Sulfur molecule. Also $\kappa_{\perp,lattice}$ (28.3 $Wm^{-1}K^{-1}$) at 20 GPa is still much smaller than $\kappa_{//,lattice}$ (96 $Wm^{-1}K^{-1}$). These facts suggest that the interlayer interaction at 20 GPa is still much weaker than the intralayer covalent bond.

Fig. 2(c) shows phonon dispersions along both cross-plane (Γ-A) and in-plane (Γ-M) directions, with group velocities indicated by a color gradient. Along the Γ-A direction, the three low-frequency optical phonon branches are close to the acoustic branches and display large dispersions, which explains the significant contribution of optical phonons to $\kappa_{\perp,lattice}$. The in-plane phonons possess much larger group velocities and phonon frequencies than cross-plane phonons; therefore, $\kappa_{//,lattice}$ is much larger than $\kappa_{\perp,lattice}$ over the entire pressure range. At ambient pressure, cross-plane optical and acoustic branches are bundled into a narrow frequency range. With increasing pressure, frequencies and group velocities of all phonon branches along Γ-A direction increase rapidly (phonon hardening effect) and their dispersions span a broader frequency range

(unbundling effect). In-plane phonons also show an increase in frequencies and group velocities. High-frequency optical phonons along all directions do not exhibit obvious change with pressure.

Larger phonon group velocity at high pressure increases the lattice thermal conductivity. The phonon unbundling effect can provide more phonon scattering channels, which could enhance phonon scattering, reduce phonon lifetimes and result in reduced thermal conductivity. The overall trend of the pressure-dependent thermal conductivity depends on these competing factors. The initial increase of $\kappa_{//,lattice}$ indicates that the phonon hardening effect dominates at lower pressures, while subsequent decrease in $\kappa_{//,lattice}$ indicates that enhanced phonon-phonon scattering dominates at higher pressures (Fig. S16).

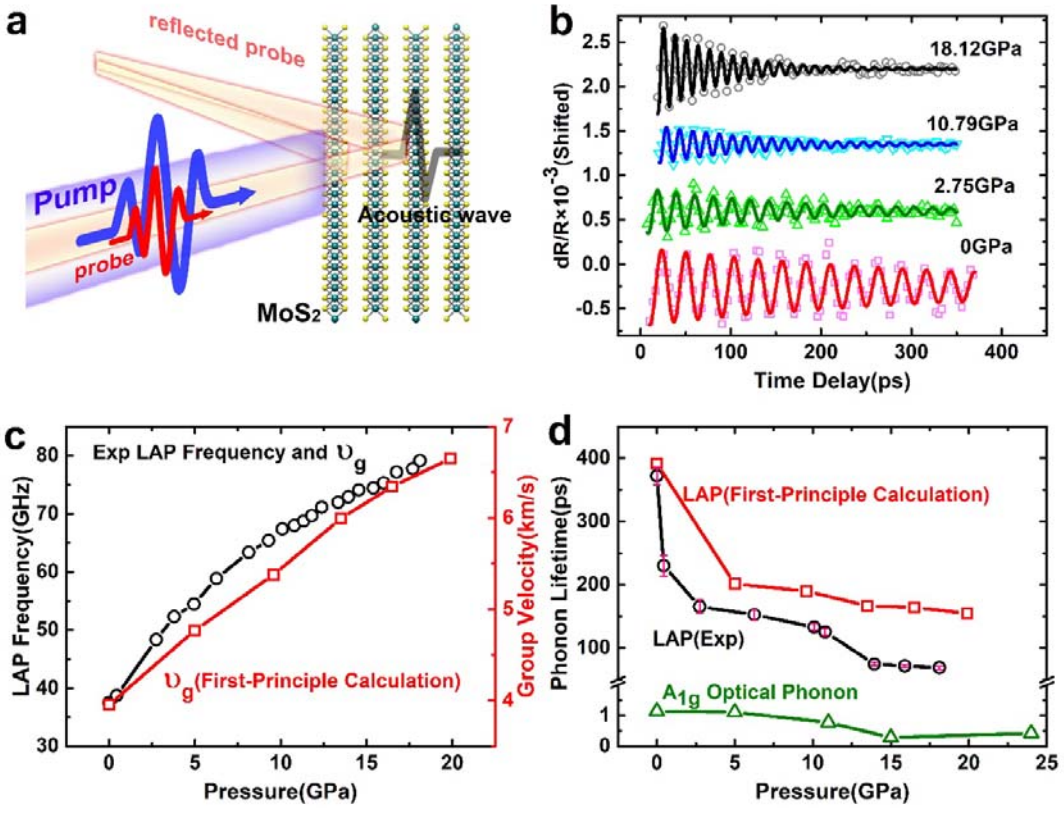


**FIG. 3. CPS measurements and first-principles calculations of phonon frequency and lifetime.** **(a)** Schematic of CPS measurements of coherent acoustic phonons in an uncoated $MoS_2$ sample. **(b)** Pressure-dependent coherent oscillations of longitudinal acoustic phonons (LAP) measured with CPS. **(c)** Pressure-dependent LAP frequencies extracted from CPS measurements (black circles) and LAP group velocities from first-principles calculations (red squares). **(d)** Pressure-dependent

LAP lifetimes extracted from CPS measurements (black circles) and from first-principles calculations (red squares), as well as lifetimes of $A_{1g}$ optical phonons extracted from Raman measurements (green triangles).

CPS was used to measure the pressure-dependent group velocity and lifetime of coherent longitudinal acoustic phonons (LAPs) along the cross-plane direction (Fig. S7). For CPS measurements, we used a 1-μm thick, bare $MoS_2$ sample roughly 100 μm in longest dimension (Fig. 3(a)). When pump pulses are absorbed at the $MoS_2$ surface, a wave packet of coherent acoustic phonons are generated and propagate into the sample. The traveling coherent phonons modify the local dielectric constants and cause partial reflection of the probe pulse (impulsive Brillouin scattering), which will interfere constructively or destructively with the reflected probe pulse from the sample surface. The oscillations shown in Fig. 3(b) correspond to coherent acoustic phonons propagating into the sample [79, 80], which can be fitted with a damped harmonic oscillator:

$$\frac{dR}{R} = A \cdot exp\left(-\frac{t}{\tau_{LAP}}\right) \cdot cos\left(2\pi f t + \varphi\right) \quad (2)$$

where $A$ is the phonon amplitude, $\tau_{LAP}$ is the phonon lifetime, $f$ is the phonon frequency and $\varphi$ is the initial phase of phonon oscillations. Phonon frequency can be converted to phonon group velocity using the relation: $v_g=\lambda f/2n$, where $\lambda$ is the probe wavelength (800 nm), and $n$ is the refractive index (4.2 for $MoS_2$) [81, 82].

Figs. 3(c-d) display the pressure-dependent phonon frequency, group velocity and lifetime of LAPs from CPS experiments and first-principles calculations. Both experimental and simulation results show that with increasing pressure, the group velocity of LAPs increases by a factor of 1.6, but phonon lifetimes are reduced by a factor of 3. Results from first-principles calculations agree with experimental observation. As discussed earlier, the increase of LAP group velocity is mainly a result of strengthened interlayer interaction and phonon hardening. The decrease of phonon lifetime relates to the intensified three-phonon (anharmonic) scattering due to phonon unbundling at high pressure [83]. When phonon dispersions spread over a broader frequency range under high pressure, revealed in Fig. 2(c), more scattering channels are available that satisfy energy and momentum

conservations simultaneously. The green symbols in Fig. 3(d) show that the lifetime of $A_{1g}$ optical phonons also decreases under high pressure (derived from our previous Raman measurements [19]), following a similar trend with LAP.

Several first-principles calculations predicted that, under tensile strain, phonon lifetime in 2D materials increases and the phonon group velocity decreases due to phonon softening [76-78]. Under compressive strain, it is reasonable to observe the opposite effect, i.e., decease of phonon lifetime and increase of phonon group velocity. Quantitatively, increase of LAP velocity and decrease of LAP lifetime could not explain the 7x increase of $\kappa_{⊡,total}$ with pressure. Nevertheless, $\kappa_{⊡,total}$ includes contributions from all phonon modes, which could not be represented by the single LAP mode detected here, and our calculated values agree well with experimental results (Fig. 1(c) and Fig. 2(a)). Based on these facts, we conclude that the drastic increase of $\kappa_{⊡,total}$ with pressure is primarily the result of strengthened interlayer forces and enhanced group velocity of LAPs. The saturation of $\kappa_{⊡,total}$ above 15 GPa is associated with the combined effects from increasing group velocity and reduced phonon lifetimes (Fig. S16).

In summary, our findings demonstrate the remarkable tunability of cross-plane thermal conductivity under extreme strain. The roughly 7x enhancement of $\kappa_{⊡,total}$ has a different physical origin than that of the electronic S-M transition reported previously, and is dominated by heavily modified phonon properties rather than electronic contributions. The electronic S-M transition begins around 10 GPa (Fig. 1(d)), where $\kappa_{⊡,total}$ has already increased from 3.5 $Wm^{-1}K^{-1}$ to about 15 $Wm^{-1}K^{-1}$(Fig. 1(c)). $MoS_2$ maintains its semiconducting nature before and during the early stage of S-M transition (< 15 GPa), where the band gap decreases from 1.03 eV to 0.2 eV and the electrical conductivity increases from 0.03 S/m to 18 S/m [19]. This study suggests that it is possible to tune electrical and thermal properties simultaneously with pressure to achieve both

high-thermal-conductivity and high-electrical-conductivity semiconducting $MoS_2$. Moreover, larger $\kappa_{⊡,total}$ will ensure that heat generated in electronic devices can be dissipated more effectively into the substrate, which will improve device performance and stability. Finally, it is conceivable that the observed phenomena should occur in most 2D materials with interlayer vdW bonding [88, 89].

**Acknowledgements**

The authors are grateful for the supports from National Science Foundation (NASCENT, Grant No. EEC-1160494; CAREER, Grant No. CBET-1351881; CBET- 1707080); Department of Energy (SBIR/STTR, Grant No. DE-SC0013178); and DOD_ Army (Grant No. W911NF-16-1-0559). AKS, TP and AS thank the Materials Research Centre and Supercomputer Education and Research Centre of Indian Institute of Science for providing computing facilities. AKS, TP and AS acknowledge support from DST Nanomission.

**Reference**


[1] X. Li, K. Maute, M. L. Dunn, and R. Yang, Phys. Rev. B **81**, 245318 (2010).
[2] N. Wei, L. Xu, H.-Q. Wang, and J.-C. Zheng, Nanotechnology **22**, 105705 (2011).
[3] Z. Ding, J.-W. Jiang, Q.-X. Pei, and Y.-W. Zhang, Nanotechnology **26**, 065703 (2015).
[4] Z. Wei, Y. Chen, and C. Dames, Appl. Phys. Lett. **102**, 011901 (2013).
[5] P. Ci *et al.*, Nano Lett. **17**, 4982 (2017).
[6] S. Bhattacharyya, T. Pandey, and A. K. Singh, Nanotechnology **25**, 465701 (2014).
[7] C.-H. Chang, X. Fan, S.-H. Lin, and J.-L. Kuo, Phys. Rev. B **88**, 195420 (2013).
[8] H. J. Conley, B. Wang, J. I. Ziegler, R. F. Haglund Jr, S. T. Pantelides, and K. I. Bolotin, Nano Lett. **13**, 3626 (2013).
[9] K. He, C. Poole, K. F. Mak, and J. Shan, Nano Lett. **13**, 2931 (2013).
[10] C. Rice, R. Young, R. Zan, U. Bangert, D. Wolverson, T. Georgiou, R. Jalil, and K. Novoselov, Phys. Rev. B **87**, 081307 (2013).
[11] A. McCreary *et al.*, ACS Nano **10**, 3186 (2016).
[12] L. Yang, X. Cui, J. Zhang, K. Wang, M. Shen, S. Zeng, S. A. Dayeh, L. Feng, and B. Xiang, Sci. Rep. **4**, 5649 (2014).
[13] A. P. Nayak *et al.*, Nano Lett. **15**, 346 (2014).
[14] Y. Wang *et al.*, Nano Res. **8**, 2562 (2015).
[15] W. Wu, J. Wang, P. Ercius, N. C. Wright, D. M. Leppert-Simenauer, R. A. Burke, M. Dubey, A. M. Dogare, and M. T. Pettes, Nano Lett. **18**, 2351 (2018).
[16] Y. Wang, C. Cong, C. Qiu, and T. Yu, Small **9**, 2857 (2013).
[17] S. Bertolazzi, J. Brivio, and A. Kis, ACS Nano **5**, 9703 (2011).
[18] W.-P. Hsieh, B. Chen, J. Li, P. Keblinski, and D. G. Cahill, Phys. Rev. B **80**, 180302 (2009).
[19] A. P. Nayak *et al.*, Nat. Commun. **5**, 4731 (2014).
[20] A. Jayaraman, Rev. Mod. Phys. **55**, 65 (1983).
[21] Z.-H. Chi, X.-M. Zhao, H. Zhang, A. F. Goncharov, S. S. Lobanov, T. Kagayama, M. Sakata, and X.-J. Chen, Phys. Rev. Lett. **113**, 036802 (2014).
[22] S. Sugai and T. Ueda, Phys. Rev. B **26**, 6554 (1982).
[23] T. Livneh and E. Sterer, Phys. Rev. B **81**, 195209 (2010).
[24] Y. Yan, F. Li, Y. Gong, M. Yao, X. Huang, X. Fu, B. Han, Q. Zhou, and T. Cui, J. Phys. Chem. C **120**, 24992 (2016).
[25] X. Li *et al.*, Appl. Phys. Lett. **109**, 242101 (2016).
[26] K. F. Mak, C. Lee, J. Hone, J. Shan, and T. F. Heinz, Phys. Rev. Lett. **105**, 136805 (2010).
[27] B. Radisavljevic, A. Radenovic, J. Brivio, i. V. Giacometti, and A. Kis, Nat. Nanotechnol. **6**, 147 (2011).
[28] J. Pu, Y. Yomogida, K.-K. Liu, L.-J. Li, Y. Iwasa, and T. Takenobu, Nano Lett. **12**, 4013 (2012).
[29] S. Kim *et al.*, Nat. Commun. **3**, 1011 (2012).
[30] W. Choi *et al.*, Adv. Mater. **24**, 5832 (2012).
[31] S. Bhattacharyya and A. K. Singh, Phys. Rev. B **86**, 075454 (2012).
[32] J. Liu, G.-M. Choi, and D. G. Cahill, J. Appl. Phys. **116**, 233107 (2014).

[33] I. Jo, M. T. Pettes, E. Ou, W. Wu, and L. Shi, Appl. Phys. Lett. **104**, 201902 (2014).
[34] S. Sahoo, A. P. Gaur, M. Ahmadi, M. J.-F. Guinel, and R. S. Katiyar, J. Phys. Chem. C **117**, 9042 (2013).
[35] C. Muratore *et al.*, Appl. Phys. Lett. **102**, 081604 (2013).
[36] J.-Y. Kim, S.-M. Choi, W.-S. Seo, and W.-S. Cho, Bull. Korean Chem. Soc. **31**, 3225 (2010).
[37] P. Jiang, X. Qian, X. Gu, and R. Yang, Adv. Mater. **29**, 1701068 (2017).
[38] Z. Ding, Q.-X. Pei, J.-W. Jiang, and Y.-W. Zhang, J. Phys. Chem. C **119**, 16358 (2015).
[39] L. Zhu, T. Zhang, Z. Sun, J. Li, G. Chen, and S. A. Yang, Nanotechnology **26**, 465707 (2015).
[40] X. Wang and A. Tabarraei, Appl. Phys. Lett. **108**, 191905 (2016).
[41] J. Chen, J. H. Walther, and P. Koumoutsakos, Nano Lett. **14**, 819 (2014).
[42] Y.-Y. Zhang, Q.-X. Pei, J.-W. Jiang, N. Wei, and Y.-W. Zhang, Nanoscale **8**, 483 (2016).
[43] J. Jeong, X. Meng, A. K. Rockwell, S. R. Bank, W.-P. Hsieh, J.-F. Lin, and Y. Wang, Nanosc Microsc Therm, 1 (2019).
[44] See Supplemental Material at [ ] for the pressure calibration in DAC, which includes Refs. [45, 46]
[45] H. Mao, J.-A. Xu, and P. Bell, J. Geophys. Res: Solid Earth **91**, 4673 (1986).
[46] A. Dewaele, M. Torrent, P. Loubeyre, and M. Mezouar, Phys. Rev. B **78**, 104102 (2008).
[47] See Supplemental Material at [ ] for the thermal physical properties and sensitivity test at high pressure, which includes Refs. [37, 48-53]
[48] C.-W. Nan, R. Birringer, D. R. Clarke, and H. Gleiter, J. Appl. Phys. **81**, 6692 (1997).
[49] G. T. Hohensee, *Using high pressure to study thermal transport and phonon scattering mechanisms* (University of Illinois at Urbana-Champaign, 2015).
[50] W.-P. Hsieh, J. Appl. Phys. **117**, 235901 (2015).
[51] K. Kusaba and T. Kikegawa, Solid State Commun. **149**, 371 (2009).
[52] S.-H. Shim, T. S. Duffy, and K. Takemura, Earth Planet. Sci. Lett. **203**, 729 (2002).
[53] J. Yang, E. Ziade, and A. J. Schmidt, Rev. Sci. Instrum. **87**, 014901 (2016).
[54] R. Mao, B. D. Kong, and K. W. Kim, J. Appl. Phys. **116**, 034302 (2014).
[55] See Supplemental Material at [ ] for thermal resistance/conductance of different interfaces, which includes Refs. [56, 57]
[56] R. Wilson, B. A. Apgar, W.-P. Hsieh, L. W. Martin, and D. G. Cahill, Phys. Rev. B **91**, 115414 (2015).
[57] H.-K. Lyeo and D. G. Cahill, Phys. Rev. B **73**, 144301 (2006).
[58] G. T. Hohensee, R. Wilson, and D. G. Cahill, Nat. Commun. **6**, 6578 (2015).
[59] W.-P. Hsieh, A. S. Lyons, E. Pop, P. Keblinski, and D. G. Cahill, Phys. Rev. B **84**, 184107 (2011).
[60] G. T. Hohensee, M. R. Fellinger, D. R. Trinkle, and D. G. Cahill, Phys. Rev. B **91**, 205104 (2015).
[61] R. Prasher, Appl. Phys. Lett. **94**, 041905 (2009).
[62] W. Jones and N. H. March, *Theoretical Solid State Physics: Perfect Lattices in Equilibrium* (Courier Corporation, 1985), Vol. 1.
[63] A. Castellanos□Gomez, M. Poot, G. A. Steele, H. S. van der Zant, N. Agraït, and G. Rubio□Bollinger, Adv. Mater. **24**, 772 (2012).
[64] See Supplemental Material at [ ] for harmonic/anharmonic interatomic force constants, phonon scattering rate, convergence check and the calculated thermal conductivity, which includes Refs. [19, 65-75]
[65] P. E. Blöchl, Phys. Rev. B **50**, 17953 (1994).

[66] G. Kresse, Phys. Rev. B **59**, 1758 (1999).
[67] G. Kresse and J. Furthmüller, Comput. Mater. Sci. **6**, 15 (1996).
[68] J. P. Perdew, A. Ruzsinszky, G. I. Csonka, O. A. Vydrov, G. E. Scuseria, L. A. Constantin, X. Zhou, and K. Burke, Phys. Rev. Lett. **100**, 136406 (2008).
[69] J. P. Perdew, K. Burke, and M. Ernzerhof, Phys. Rev. Lett. **77**, 3865 (1996).
[70] S. Grimme, J. Antony, S. Ehrlich, and H. Krieg, J. Chem. Phys. **132**, 154104 (2010).
[71] A. Togo and I. Tanaka, Scripta Mater. **108**, 1 (2015).
[72] A. Togo, F. Oba, and I. Tanaka, Phys. Rev. B **78**, 134106 (2008).
[73] N. Wakabayashi, H. Smith, and R. Nicklow, Phys. Rev. B **12**, 659 (1975).
[74] W. Li, J. Carrete, N. A. Katcho, and N. Mingo, Comput. Phys. Commun. **185**, 1747 (2014).
[75] W. Li, L. Lindsay, D. Broido, D. A. Stewart, and N. Mingo, Phys. Rev. B **86**, 174307 (2012).
[76] S.-D. Guo and J. Dong, J. Phys. D: Appl. Phys. **51**, 265307 (2018).
[77] Y. Kuang, L. Lindsay, and B. Huang, Nano Lett. **15**, 6121 (2015).
[78] H. Liu, G. Qin, Y. Lin, and M. Hu, Nano Lett. **16**, 3831 (2016).
[79] F. He, W. Wu, and Y. Wang, Appl. Phys. A **122**, 777 (2016).
[80] W. Wu and Y. Wang, Opt. Lett. **40**, 64 (2015).
[81] C. Yim, M. O'Brien, N. McEvoy, S. Winters, I. Mirza, J. G. Lunney, and G. S. Duesberg, Appl. Phys. Lett. **104**, 103114 (2014).
[82] C. Thomsen, H. T. Grahn, H. J. Maris, and J. Tauc, Phys. Rev. B **34**, 4129 (1986).
[83] See Supplemental Material at [ ] for the estimation of penetration depth at high pressure proving our observation is not from the artificial effect that LAP travels out of probing region but from the reduction of phonon lifetime, which includes Refs. [84-87]
[84] C. Roxlo, R. Chianelli, H. Deckman, A. Ruppert, and P. Wong, J. Vac. Sci. Technol., A **5**, 555 (1987).
[85] E. Fortin and W. Sears, J. Phys. Chem. Solids **43**, 881 (1982).
[86] Y. Tsay, S. Mitra, and B. Bendow, Phys. Rev. B **10**, 1476 (1974).
[87] A. Dewaele, J. Eggert, P. Loubeyre, and R. Le Toullec, Phys. Rev. B **67**, 094112 (2003).
[88] A. P. Nayak *et al.*, ACS Nano **9**, 9117 (2015).
[89] B. Liu *et al.*, J. Phys. Chem. C **114**, 14251 (2010).